Hydrogen production by steam reforming of liquefied natural gas (LNG) over mesoporous Ni/Al$_2$O$_3$ catalyst prepared by an EDTA-assisted impregnation method

Yongju Bang, Seungwon Park, Seung Ju Han, Jaekyeong Yoo, Ji Hwan Song, Jung Ho Choi, Ki Hyuk Kang, In Kyu Song*

School of Chemical and Biological Engineering, Institute of Chemical Processes, Seoul National University, Shinlim-dong, Kwanak-ku, Seoul 151-744, South Korea

ARTICLE INFO

ABSTRACT

A mesoporous alumina (denoted as MA) support was prepared by an epoxide-driven sol-gel method. A mesoporous Ni/Al$_2$O$_3$ catalyst was then prepared via impregnation of Ni(EDTA)$^{2-}$ complex anions onto positively-charged mesoporous alumina support (denoted as NiE/MA). For comparison, a mesoporous Ni/Al$_2$O$_3$ catalyst was also prepared by introducing nickel species onto MA support via conventional impregnation method (denoted as Ni/MA). Both NiE/MA and Ni/MA catalysts were applied to the hydrogen production by steam reforming of liquefied natural gas (LNG) in order to investigate the effect of preparation method on the catalytic performance. Ni/MA catalyst retained relatively large amount of nickel species in the form of bulk nickel oxide, which were weakly bound to alumina support compared to NiE/MA catalyst. It was found that the reduced NiE/MA catalyst showed smaller metallic nickel particle size and higher nickel dispersion than the reduced Ni/MA catalyst, implying that NiE/MA catalyst retained stronger resistance toward nickel sintering than Ni/MA catalyst during the reduction process. It was also revealed that methane adsorption capacity of the reduced NiE/MA catalyst was larger than that of the reduced Ni/MA catalyst. NiE/MA catalyst with larger methane adsorption capacity exhibited better catalytic performance than Ni/MA catalyst in the hydrogen production by steam reforming of LNG.

© 2015 Elsevier B.V. All rights reserved.

1. Introduction

Research developments for utilization of alternative energies have become a major challenging issue in these days due to increasing environmental problems such as air pollution, water pollution, ozone layer depletion, and global warming [1–5]. It is well known that hydrogen can serve as a renewable energy carrier due to its non-polluting nature [6,7]. Furthermore, several hydrogen application areas including fuel cell, ammonia synthesis, hydrogenation processes have triggered the development of hydrogen production technologies [8]. Hydrogen can be mainly produced by fuel processing of hydrocarbons (methane, ethane), alcohols (methanol, ethanol), and bio-derived compounds (acetic acid, glycerol), although there are other early-stage hydrogen production technologies such as electrolysis and photo-catalytic water splitting [9–13]. In particular, steam reforming of methane has been widely employed to large-scale hydrogen production due to its economic feasibility. When considering the growing atten-

tion toward abundant reserves of natural gas (or shale gas), which is mainly composed of methane, steam reforming of liquefied natural gas (LNG) can be a promising route for stable hydrogen production. Both well-established LNG supply infrastructures and wide-spreading LNG pipelines in the modern cities are expected to make on-site hydrogen production efficient.

Various reforming catalysts such as Rh [14,15], Ru [16,17], Pd [18,19], Pt [20,21], Co [22,23], and Ni [24–26] have been extensively investigated. Among these catalysts, nickel-based catalysts have been widely used for hydrogen production by steam reforming reaction. However, the nickel-based catalysts with poor nickel dispersion prepared by an impregnation method are not only unfavorable for efficient hydrogen production but also vulnerable to catalyst deactivation caused by sintering and carbon deposition. Therefore, many attempts such as co-precipitation [27], sol–gel processing [28,29], templating [30,31], and promoter addition [32–34] have been made to enhance catalytic activity and stability of the nickel-based catalysts in the steam reforming reaction by increasing nickel dispersion of the catalysts.

Transition metal species exist as a form of M^{n+} cations in most cases of impregnation solution. These metal cations are impregnated onto metal oxide support via drying and calcination steps,

* Corresponding author. Fax: +82 2 889 7415.
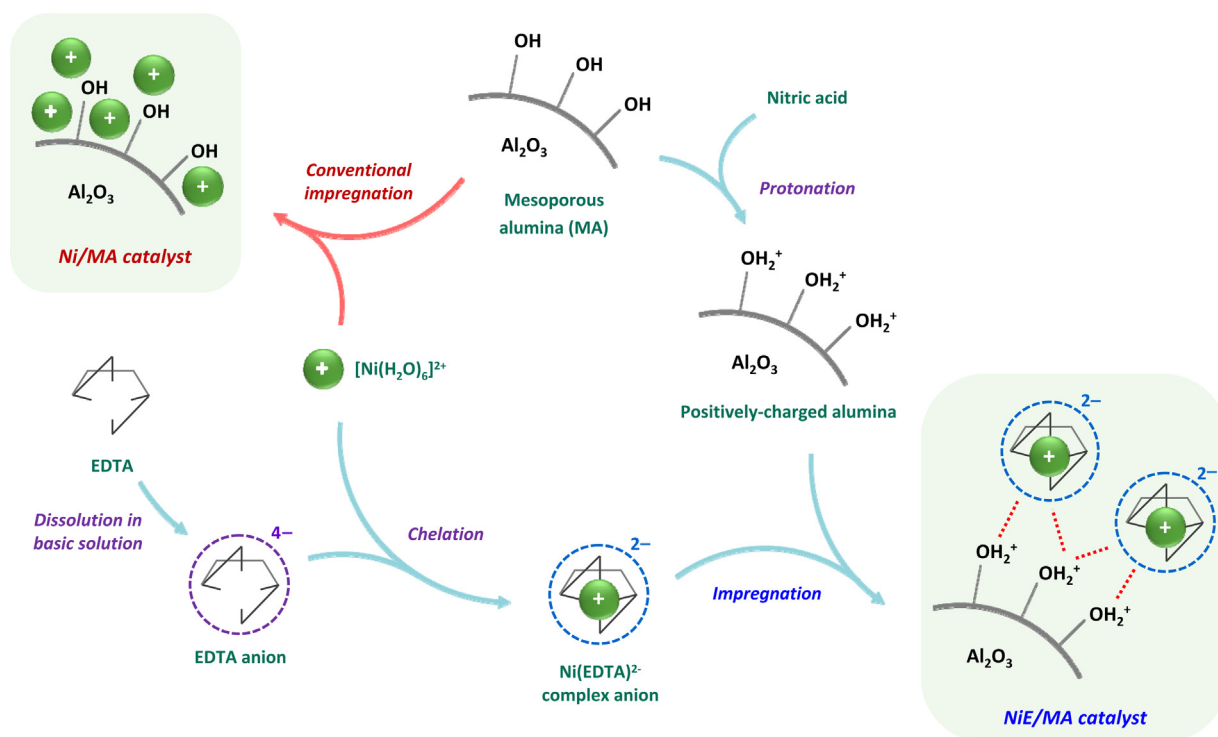*E-mail address:* inksong@snu.ac.kr (I.K. Song).

Fig. 1. Schematic procedures for the preparation of NiE/MA and Ni/MA catalysts.

resulting in poor metal dispersion on the support due to severe aggregation of metal species. It is interesting to note that some researches, in which metal species were introduced onto metal oxide support by means of a chelating agent such as ethylene-diaminetetraacetic acid (EDTA), have been attempted to enhance metal dispersion on the support [35–37]. To our best knowledge, however, no research has been made on the direct impregnation of chelated nickel species onto positively-charged mesoporous alumina support. Only a few investigations such as metal loading on metal oxide by chelation [35], impregnation of metal ions onto EDTA-bound alumina support [36], and addition of chelated metal anions into hydrotalcite structure [37] were carried out so far. Therefore, an investigation on the mesoporous Ni/Al_2O_3 steam reforming catalyst prepared by introducing chelated nickel species onto positively-charged mesoporous alumina support would be worthwhile.

In this work, a mesoporous Ni/Al_2O_3 catalyst was prepared by an EDTA-assisted impregnation method. For comparison, a mesoporous Ni/Al_2O_3 catalyst was also prepared by a conventional impregnation method. The EDTA-assisted impregnation method is expected to be efficient in terms of metal-support interaction between nickel species and alumina support, nickel dispersion, and methane adsorption capacity of Ni/Al_2O_3 catalyst compared to the conventional impregnation method. Several characterizations such as N_2 adsorption–desorption, XRD, TPR, TEM, H_2–TPD, and CH_4–TPD were conducted to elucidate the physicochemical properties of the prepared catalysts.

2. Experimental

2.1. Preparation of mesoporous alumina support by an epoxide-driven sol–gel method

A mesoporous alumina support was prepared by an epoxide-driven sol–gel method according to the similar methods reported in the previous studies [29,38–40]. 11.4 g of aluminum precursor (aluminum nitrate nonahydrate, Sigma–Aldrich) was dissolved in 80 ml of anhydrous ethanol with vigorous stirring. For sufficient hydration of metal species, 1.6 ml of distilled water was then added to the solution. 21.4 ml of propylene oxide (Sigma–Aldrich), which acted as a gelation agent, was introduced into the solution to generate hydroxyl groups on metal species and to induce condensation reaction between metal species. After stirring the solution for several minutes, a white wet gel was obtained. The gel was aged for 2 days, and then it was dried at 70 °C for 2 days. The resulting powder was finally calcined at 700 °C for 5 h to yield a mesoporous alumina support (denoted as MA).

2.2. Preparation of nickel catalyst supported on mesoporous alumina support by an EDTA-assisted impregnation method

A mesoporous Ni/Al_2O_3 catalyst was prepared by an EDTA-assisted impregnation method. Fig. 1 shows the schematic procedures for the catalyst preparation. Nickel precursor solution was prepared by dissolving 2.0 g of nickel precursor (nickel nitrate hexahydrate, Sigma–Aldrich) in 1.5 ml of distilled water (Solution A). 2.0 g of EDTA (ethylenediaminetetraacetic acid, Sigma–Aldrich) was added in 11.5 ml of distilled water (Solution B). In order for complete dissolution of EDTA, pH of Solution B was kept at 8.0 by introducing ammonia solution (Solution C). Solution A was then added into the solution C dropwise to prepare a blue-colored Ni–EDTA complex solution (Solution D). Here, pH of Solution D was maintained at 8.0.

1.0 g of mesoporous alumina support (MA) was dispersed in 10 ml of distilled water (Mixture E). Nitric acid was then added dropwise into the Mixture E until pH 4, which was less than predetermined pH_{zpc} (zpc: zero point of charge) value of MA support, to induce positive charge on the MA support by protonating hydroxyl groups (Mixture F). The solution D was then slowly introduced to the Mixture F for impregnation of nickel species onto MA support (Mixture G). The Mixture G was heated at 100 °C and stirred for the removal of solvent. The resulting powder was then addition-
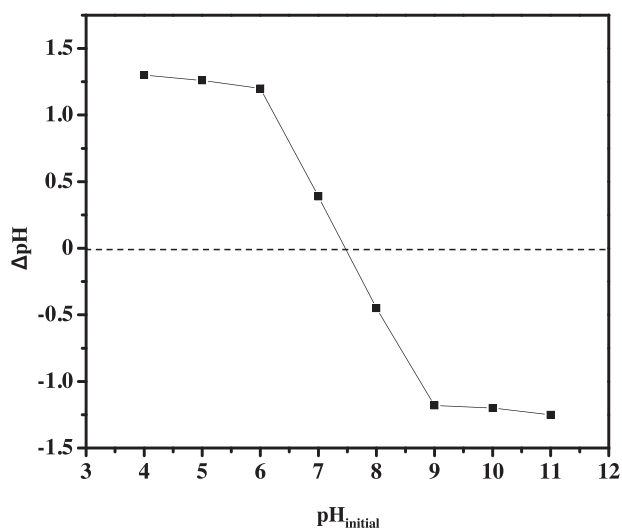
Fig. 2. ΔpH value plotted as a function of $pH_{initial}$ for the determination of pH_{zpc} value on MA support.

ally dried at 100 °C overnight, and subsequently, it was calcined at 700 °C for 5 h. The resulting nickel catalyst impregnated on mesoporous alumina support was denoted as NiE/MA.

For comparison, a mesoporous Ni/Al$_2$O$_3$ catalyst was also prepared by a conventional impregnation method using MA support and aqueous solution of nickel nitrate hexahydrate (denoted as Ni/MA). Drying and calcination conditions of Ni/MA catalyst were identical to those of NiE/MA catalyst. Nickel loading was kept at 40 wt% in both NiE/MA and Ni/MA catalysts.

2.3. Determination of pH_{zpc} value on mesoporous alumina support

The pH_{zpc} (zpc: zero point of charge) value of mesoporous alumina support (MA) was determined by a batch equilibration method as described in the literature [41]. 25 mg of MA support was dispersed in 25 ml of 0.1 M KNO$_3$ aqueous solution with vigorous stirring for 10 min. Eight bottles of above solution were prepared and initial pH ($pH_{initial}$) of each bottle was adjusted to 4, 5, 6, 7, 8, 9, 10, and 11 using aqueous solution of HNO$_3$ or NaOH. After keeping the solution for 12 h, final pH (pH_{final}) of the solution was measured. The ΔpH value (the difference between $pH_{initial}$ and pH_{final}) was plotted as a function of $pH_{initial}$ as presented in Fig. 2. Finally, the pH_{zpc} value (ca. 7.5) of MA support was determined at the point of ΔpH 0.

2.4. Characterization

Textural properties of support (MA) and catalysts (NiE/MA and Ni/MA) were examined by nitrogen adsorption–desorption analyses at 77 K using a BELSORP-mini II (BEL Japan) apparatus. Prior to the analyses, all the samples were degassed at 150 °C for 6 h using a vacuum pump to desorb moisture and other gases on the surface of samples. Surface areas of the samples were determined according to the Brunauer–Emmett–Teller (BET) equation.

To examine Ni loading of the catalysts, ICP–AES analyses were carried out using an ICPS-1000IV (Shimadzu) instrument. Each catalyst was pretreated with a mixture of nitric acid and hydrochloric acid (1:3 volume ratio). The metal solution was then mixed with deionized water and heated to dissolve metal species completely.

X-ray diffraction (XRD) analyses were performed to investigate the crystalline structures of calcined and reduced catalysts using a D-Max2500-PC (Rigaku) diffractometer. During the analy-

ses, operating voltage and current were kept as 50 kV and 150 mA, respectively. XRD patterns were collected within the range of $2\theta = 20$–$80°$ with a scan rate of 10°/min under Cu-Kα radiation ($\lambda = 1.541$ Å). 20 mg of each calcined catalyst was preliminarily reduced at 700 °C for 3 h under H$_2$ flow (3 ml/min) diluted with N$_2$ flow (30 ml/min) for XRD analysis of reduced catalyst.

Temperature-programmed reduction (TPR) analyses were carried out in order to investigate metal-support interaction between nickel and alumina species in the catalysts. Each calcined catalyst (50 mg) was loaded into a U-shaped quartz cell, and then it was reduced within the temperature range of room temperature–1000 °C with a heating rate of 5 °C/min under a mixed stream of H$_2$ flow (2 ml/min) and N$_2$ flow (20 ml/min). TPR profiles were recorded using a thermal conductivity detector (TCD). TPR analyses of reduced catalysts were also conducted to examine the degree of reduction of the reduced catalysts according to the similar method for TPR analyses of calcined catalysts, except that 50 mg of each calcined catalyst was preliminarily reduced at 700 °C for 3 h under H$_2$ flow (3 ml/min) diluted with N$_2$ flow (30 ml/min) before the analysis. Morphological features of reduced catalysts were examined by transmission electron microscopy (TEM) analyses using a JEM-2100 (Jeol) electron microscope with an accelerating voltage of 200 kV. For TEM analyses of reduced catalysts, 20 mg of each calcined catalyst was ex-situ reduced under H$_2$ flow (3 ml/min) diluted with N$_2$ flow (30 ml/min) at 700 °C for 3 h before the analysis.

Hydrogen temperature-programmed desorption (H$_2$–TPD) analyses were carried out using a BELCAT-B (BEL Japan) instrument equipped with a TCD in order to calculate nickel surface area and nickel dispersion of reduced catalysts. 20 mg of each catalyst was charged into a quartz cell, and it was reduced at 700 °C for 3 h with 5% H$_2$/Ar flow (50 ml/min). After cooling the cell to 50 °C under Ar flow (50 ml/min), the cell was treated with 5% H$_2$/Ar flow (50 ml/min) for 30 min to saturate the catalyst surface with hydrogen. The cell was then purged at 100 °C for 1 h under Ar flow (50 ml/min). After cooling the cell to 50 °C, H$_2$–TPD analysis was conducted by increasing the cell temperature from 50 °C to 1000 °C with a heating rate of 10 °C/min.

To evaluate methane adsorption capacity of reduced catalysts, methane temperature-programmed desorption (CH$_4$–TPD) analyses were conducted. 20 mg of each catalyst was charged into a U-shaped quartz cell, and it was reduced at 700 °C for 3 h with H$_2$ flow (3 ml/min) diluted with He flow (30 ml/min). The cell was cooled to room temperature and purged with He flow (30 ml/min). After the pulse injection (10 times) of methane (20 ml) into the cell under He flow (5 ml/min), the cell was treated at 100 °C for 1 h under He flow (30 ml/min). CH$_4$–TPD analysis was then conducted by increasing cell temperature from room temperature to 800 °C with a heating rate of 10 °C/min under a mixed flow of H$_2$ (2 ml/min) and He (10 ml/min). Outlet gases were analyzed using a mass selective detector (5975 MSD, Agilent).

CHNS elemental analyses were carried out to determine the amount of carbon deposition on the spent catalysts using a TruSpec Micro CHNS (Leco) apparatus.

2.5. Catalytic test

In order to assess catalytic performance of NiE/MA and Ni/MA catalysts in the hydrogen production by steam reforming of LNG, both catalysts were tested in a fixed-bed flow reactor. 20 mg of each catalyst was charged into a quartz reactor, and it was in-situ reduced at 700 °C for 3 h under H$_2$ flow (3 ml/min) diluted with N$_2$ flow (30 ml/min). After cooling the reactor to reaction temperature (550 °C or 800 °C) with N$_2$ flow (30 ml/min), steam reforming of LNG was conducted. Simulated LNG flow (CH$_4$: 4.6 ml/min + C$_2$H$_6$: 0.4 ml/min) diluted with N$_2$ flow (30 ml/min)
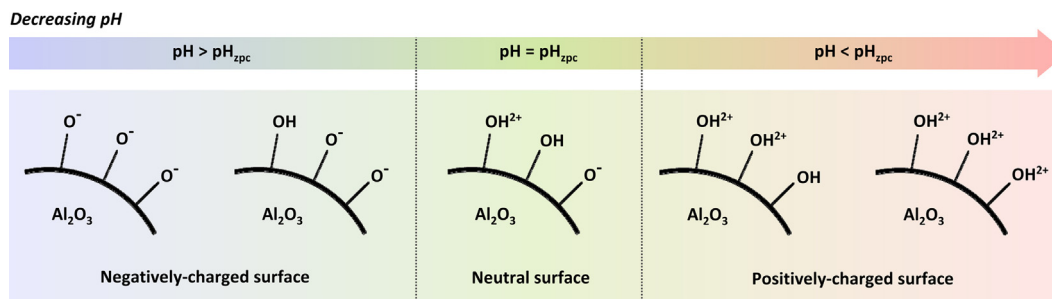
Fig. 3. Surface modification of alumina by changing pH.

was supplied into the reactor together with steam (11.3 ml/min) to keep the steam/carbon molar ratio at 2.09. Outlet gases produced from the reactor were analyzed with an on-line gas chromatograph (ACME 6000, Younglin) equipped with a TCD. Catalytic performance in terms of LNG conversion and hydrogen yield was calculated according to the following equations.

$$\text{LNG conversion(\%)} = \left(1 - \frac{F_{\text{CH}_4,\text{out}} + F_{\text{C}_2\text{H}_6,\text{out}}}{F_{\text{CH}_4,\text{in}} + F_{\text{C}_2\text{H}_6,\text{in}}}\right) \times 100 \qquad (1)$$

$$\text{Hydrogen yield(\%)} = \frac{F_{\text{H}_2,\text{out}}}{4 \times F_{\text{CH}_4,\text{in}} + 7 \times F_{\text{C}_2\text{H}_6,\text{in}}} \times 100 \qquad (2)$$

3. Results and discussion

3.1. EDTA-assisted impregnation method

Detailed description for EDTA-assisted impregnation method, which was employed for the preparation of NiE/MA catalyst in this study, can be summarized as follows. In the EDTA-assisted impregnation method, the Coulombic interaction between positively-charged hydroxyl groups ($-\text{OH}^{2+}$) and Ni(EDTA)$^{2-}$ complex anions is utilized to impregnate nickel species on mesoporous alumina support (MA). In general, mesoporous alumina support contains many hydroxyl groups ($-\text{OH}$) on the surface. The charge of these hydroxyl groups can be modified by changing pH of alumina-dispersed liquid as reported in the literature [36]. As shown in Fig. 3, hydroxyl groups on the alumina support are gradually protonated with decreasing pH of the alumina-dispersed liquid. In detail, the amount of positively-charged hydroxyl groups is large when pH of the alumina-dispersed liquid is lower than pH$_{zpc}$ of the alumina, because protons in the liquid are bound to hydroxyl group on the alumina surface. When pH of the alumina-dispersed liquid is higher than pH$_{zpc}$ of the alumina, on the contrary, protons bound to hydroxyl groups tend to be separated from the alumina, resulting in the decreased amount of positively-charged hydroxyl groups. In order to generate positive charge on the MA support, therefore, pH of the alumina-dispersed liquid (Mixture E in Section 2.2) was lowered than predetermined pH$_{zpc}$ value (ca. 7.5) of MA support.

According to the theoretical background [42], it is known that formation constant (K_f) of chelated Ni(EDTA)$^{2-}$ complex anion from free Ni^{2+} ion and EDTA^{4-} ion is $10^{18.4}$ (Eqs. (3) and (4)). Furthermore, molar fraction (α) of EDTA^{4-} ion among all types of EDTA molecules (H$_6$EDTA^{2+}, H$_5$EDTA$^+$, H$_4$EDTA, H$_3$EDTA$^-$, H$_2$EDTA^{2-}, HEDTA^{3-}, and EDTA^{4-}) is known to be 0.0042 at pH 8. Accordingly, molar concentrations of chelated Ni(EDTA)$^{2-}$ complex anion and free Ni^{2+} ion in the Ni–EDTA complex solution (Solution D in Section 2.2) can be calculated by the following equations.
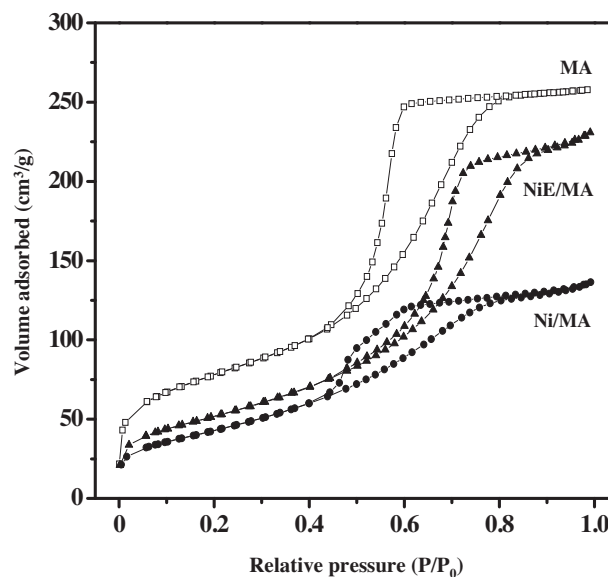
$$\text{Ni}^{2+} + \text{EDTA}^{4-} \xrightarrow{K_f} \text{Ni(EDTA)}^{2-} \qquad (3)$$

Fig. 4. Nitrogen adsorption–desorption isotherms of calcined support (MA) and catalysts (NiE/MA and Ni/MA).

$$K_f = \frac{\left[\text{Ni(EDTA)}^{2-}\right]}{\left[\text{Ni}^{2+}\right]\left[\text{EDTA}^{4-}\right]} \qquad (4)$$

$$\left[\text{EDTA}^{4-}\right] = \alpha\,[\text{EDTA}] \qquad (5)$$

From the above equations, molar concentrations of chelated Ni(EDTA)$^{2-}$ complex anion and free Ni^{2+} ion were found to be 3.1×10^{-1} M and 5.4×10^{-9} M, respectively. Thus, the degree of chelation for nickel ions was greater than 99%. In other words, most of nickel ions in the Ni–EDTA complex solution (Solution D in Section 2.2) can be chelated by EDTA molecules. Therefore, it is inferred that nickel species can be impregnated onto MA support via the Coulombic interaction between positively-charged hydroxyl groups and chelated Ni(EDTA)$^{2-}$ complex anions during the preparation of NiE/MA catalyst.
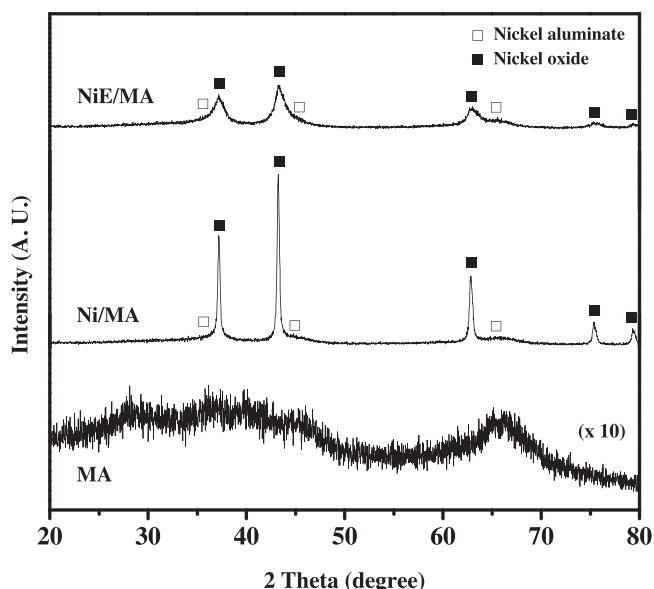
3.2. Textural properties

Nitrogen adsorption–desorption isotherms of calcined support (MA) and catalysts (NiE/MA and Ni/MA) are presented in Fig. 4. All the calcined samples exhibited IV-type isotherms with H2-type hysteresis loops, indicating that a well-developed mesoporous structure with "ink-bottle" shape was formed in the samples [43]. It was observed that NiE/MA and Ni/MA catalysts showed smaller nitrogen adsorption than MA support. This indicates that the mesoporous structure of MA support was significantly blocked by nickel species during the impregnation step for NiE/MA catalyst and during the impregnation step for Ni/MA catalyst. However,

Table 1
Textural properties of calcined support (MA) and catalysts (NiE/MA and Ni/MA).

Sample	Ni loading (wt%)[a]	Surface area (m²/g)[b]	Pore volume (cm³/g)[c]	Pore diameter (nm)
MA	–	278	0.40	5.7
NiE/MA	40	188	0.36	7.6
Ni/MA	40	157	0.21	5.4

[a] Determined by ICP–AES analyses.
[b] Calculated by the BET equation.
[c] Total pore volume at P/P_0 ~0.995.

Fig. 5. XRD patterns of calcined support (MA) and catalysts (NiE/MA and Ni/MA).

Fig. 6. TPR profiles of calcined NiE/MA and Ni/MA catalysts.

NiE/MA catalyst showed larger nitrogen adsorption than Ni/MA catalyst. This is because nickel species of NiE/MA catalyst were less aggregated on positively-charged MA support via EDTA-assisted impregnation compared to those of Ni/MA catalyst.

Table 1 summarizes the textural properties of calcined support (MA) and catalysts (NiE/MA and Ni/MA). All the calcined samples retained mesopores larger than 5 nm. Surface area and pore volume of calcined NiE/MA and Ni/MA catalysts were significantly decreased compared to those of MA support due to pore blockage by nickel species. However, NiE/MA catalyst showed higher surface area, larger pore volume, and larger pore diameter than Ni/MA catalyst. During the impregnation step of NiE/MA catalyst, Ni(EDTA)²⁻ complex anions are bound to positively-charged hydroxyl groups (−OH²⁺) on the MA support by forming the strong Coulombic interaction. On the other hand, Ni²⁺ ions are introduced onto MA support without attractive interaction during the impregnation step of Ni/MA catalyst, resulting in large aggregates of nickel species in the Ni/MA catalyst. These large aggregates block surface and mesopores of Ni/MA catalyst.

3.3. Crystalline structure and reduction behavior of calcined catalysts

XRD patterns of calcined support (MA) and catalysts (NiE/MA and Ni/MA) are shown in Fig. 5. MA support showed a broad and amorphous pattern, implying that dehydroxylation process of as-prepared alumina xerogel was considerably restrained by mesoporous structure [44]. As shown in Fig. 5, it was observed that both NiE/MA and Ni/MA catalysts exhibited nickel aluminate phase, which was generated from interaction between alumina and nickel species [45], as well as nickel oxide phase. Interestingly, diffraction peaks for nickel oxide phase in the Ni/MA catalyst were sharper

than those in the NiE/MA catalyst, implying that nickel oxide phase in the Ni/MA catalyst was more crystallized than that in the NiE/MA catalyst. This is because significantly aggregated nickel species in the Ni/MA catalyst were vulnerable to crystallization and sintering during the calcination step. It is inferred that most of nickel species with poor dispersion in the Ni/MA catalyst were transformed into bulk nickel oxide phase and that only a small amount of nickel species was crystallized into nickel aluminate phase or nickel oxide strongly interacted with alumina support. On the other hand, most of nickel species in the NiE/MA catalyst were crystallized into nickel aluminate phase or nickel oxide strongly interacted with alumina support due to effective atomic diffusion based on intimate contact of nickel species with alumina.

TPR behaviors of calcined NiE/MA and Ni/MA catalysts were investigated as shown in Fig. 6. NiE/MA and Ni/MA catalysts showed a reduction band at 691 °C and 728 °C, respectively, which corresponded to the reduction of nickel aluminate phase or nickel oxide phase strongly interacted with γ-Al₂O₃ [46,47]. These types of nickel species are known to be relatively stable toward nickel sintering during the reduction process compared to bulk nickel oxide phase, because their atomic or crystallite migration of nickel species on γ-Al₂O₃ surface might be significantly prevented by metal–support interaction [48]. It is interesting to note that another reduction band at 382 °C, which was ascribed to the reduction of bulk nickel oxide phase, was detected in the TPR profile of Ni/MA catalyst. The bulk nickel oxide phase weakly interacted with γ-Al₂O₃ support in the Ni/MA catalyst was expected to be easily sintered to large metallic nickel crystallite during the reduction process. It was also found that Ni/MA catalyst exhibited relatively broad reduction profile within the temperature range of
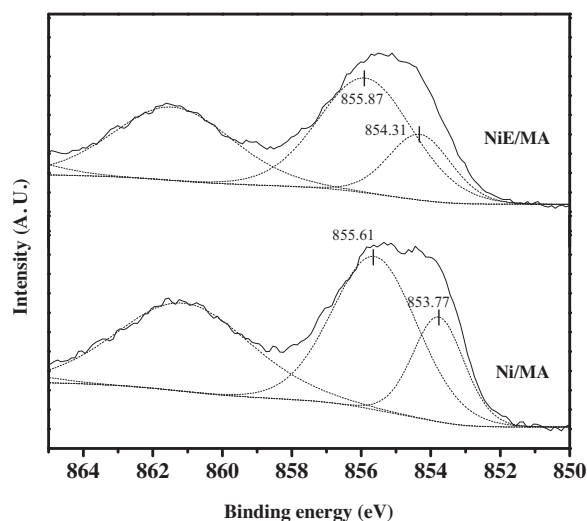
Fig. 7. XPS spectra in the Ni 2p level of calcined NiE/MA and Ni/MA catalysts.

Table 2
Degree of reduction and particle size of metallic nickel in the reduced NiE/MA and Ni/MA catalysts.

Catalyst	Degree of reduction (%)[a]	Particle size of metallic nickel	
		XRD (nm)[b]	TEM (nm)[c]
NiE/MA	>99	10	13
Ni/MA	>99	30	34

[a] Calculated by following equation:

$$\text{Degree of reduction}(\%) = \left(\frac{\text{TPR peak area for calcined catalyst–TPR peak area for reduced catalyst}}{\text{TPR peak area for calcined catalyst}} \right) \times 100$$

Peak areas were calculated from Figs. 6 and 8.
[b] Calculated by the Scherrer equation from Ni (2 0 0) diffraction peak broadening in Fig. 9.
[c] Average value of 100 nickel particles in TEM images of Fig. 10(a) and (b).

330–850 °C compared to NiE/MA catalyst. This broad reduction profile of Ni/MA catalyst implies that nickel species in the Ni/MA catalyst were less uniform than those in the NiE/MA catalyst. Thus, it is inferred that Ni/MA catalyst would retain a broader particle size distribution than NiE/MA catalyst after the reduction process.

The above results were further confirmed by XPS analyses as shown in Fig. 7. Both NiE/MA and Ni/MA catalysts exhibited two deconvoluted Ni 2p level peaks; the peak at 855–856 eV was due to nickel aluminate phase, while the peak at 853–855 eV was attributed to nickel oxide phase [49]. It was observed that binding energies for two peaks of NiE/MA catalyst were higher than those of Ni/MA catalyst. This indicates that nickel species in the NiE/MA catalyst are more intimately interacting with alumina support than those in the Ni/MA catalyst. It should also be noted that binding energy difference between high binding energy peak and low binding energy peak in the Ni/MA catalyst was larger than that in the NiE/MA catalyst, due to low uniformity of nickel species in the Ni/MA catalyst. Thus, it can be summarized that Ni/MA catalyst retained relatively large amount of nickel species in the form of bulk nickel oxide, which were weakly bound to γ-Al₂O₃ support compared to NiE/MA catalyst.

3.4. Crystalline structure and nickel dispersion of reduced catalysts

In order to determine the degree of reduction for NiE/MA and Ni/MA catalysts reduced at 700 °C for 3 h, TPR analyses of reduced catalysts were carried out as presented in Fig. 8. As listed in Table 2, it was revealed that the degree of reduction for both reduced NiE/MA and Ni/MA catalysts was higher than 99%, representing that
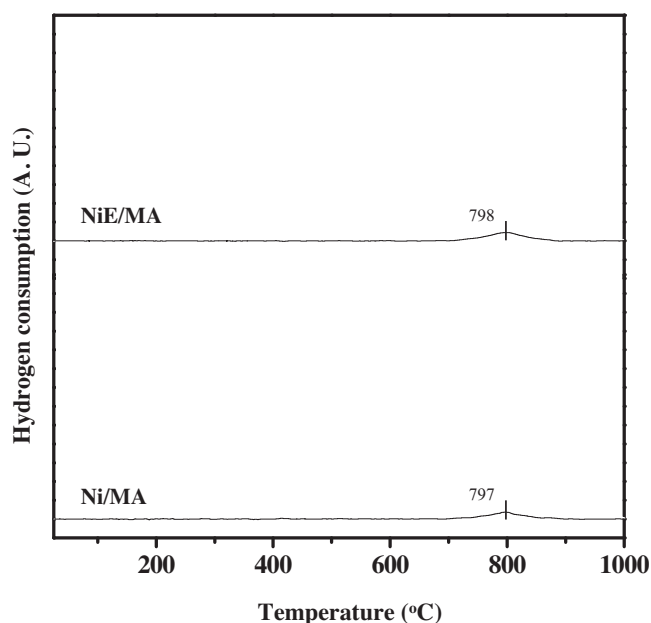

Fig. 8. TPR profiles of reduced NiE/MA and Ni/MA catalysts.
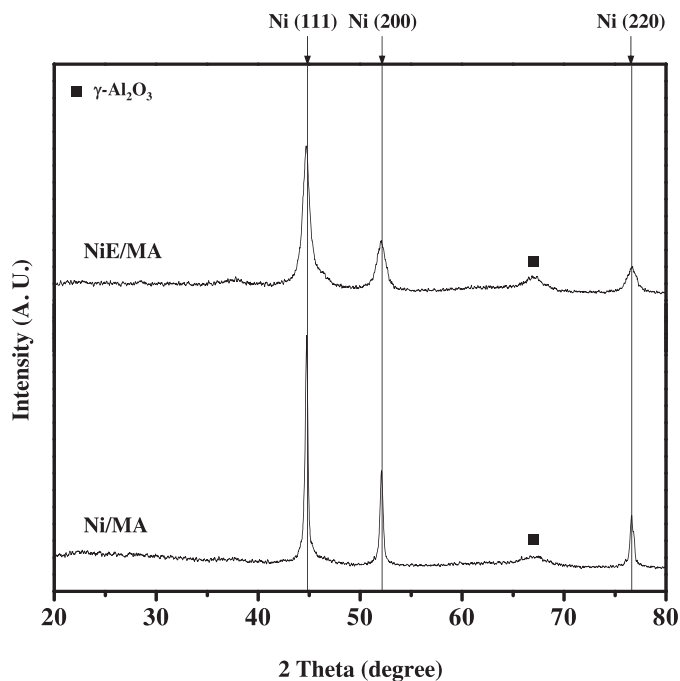

Fig. 9. XRD patterns of reduced NiE/MA and Ni/MA catalysts.

the reduction condition (700 °C for 3 h) employed in this study was sufficient for reducing almost all nickel species in the catalysts.

Fig. 9 shows the XRD patterns of reduced NiE/MA and Ni/MA catalysts. Both NiE/MA and Ni/MA catalysts retained metallic nickel phase and γ-Al₂O₃ phase after the reduction process. In addition, no distinct diffraction peaks corresponding to nickel oxide or nickel aluminate phases were detected in both catalysts. These were well consistent with the result that both reduced NiE/MA and Ni/MA catalysts exhibited a high degree of reduction (ca. 100%). Interestingly, the reduced Ni/MA catalyst showed sharper diffraction peaks corresponding to metallic nickel phase than the reduced NiE/MA catalyst, indicating that nickel species reduced from nickel oxide phase and nickel aluminate phase in the calcined Ni/MA catalyst
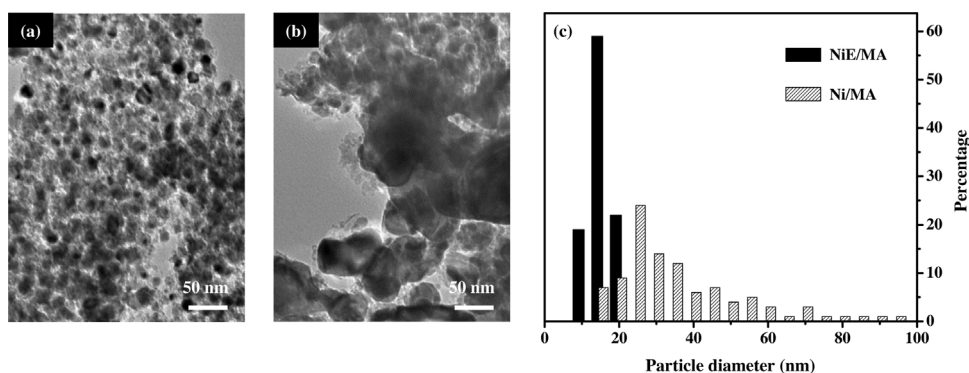
Fig. 10. TEM images of reduced (a) NiE/MA catalyst and (b) Ni/MA catalyst, and (c) particle size distributions of the reduced catalysts.

Table 3
H$_2$–TPD results of reduced NiE/MA and Ni/MA catalysts.

Catalyst	Amount of adsorbed hydrogen (μmol H$_2$/g)[a]				Nickel surface area (m^2/g Ni)[b]	Nickel dispersion (%)[b]	Average nickel diameter (nm)[b]
	Weak hydrogen-binding site (<200 °C)	Medium hydrogen-binding site (200–400 °C)	Strong hydrogen-binding site (400–500 °C)	Total			
NiE/MA	20.5 (15.9%)	49.5 (38.6%)	58.5 (45.5%)	128.5	35.2	5.3	19
Ni/MA	9.1 (13.3%)[c]	21.5 (31.5%)	37.7 (55.2%)	68.3	18.7	2.8	36

[a] Calculated from deconvoluted peak area of H$_2$–TPD profiles in Fig. 11.

[b] Calculated by assuming H/Ni$_{atom}$ = 1

[c] Values in parentheses are percentage of each deconvoluted area in H$_2$–TPD profiles.

were susceptible to nickel sintering compared to those in the calcined NiE/MA catalyst. This result was due to more uniform and stronger metal–support interaction in the calcined NiE/MA catalyst than in the calcined Ni/MA catalyst as discussed in TPR results of calcined catalysts (Fig. 6). Particle size of metallic nickel in the reduced catalysts was determined by the Scherrer equation as listed in Table 2. It was found that the reduced Ni/MA catalyst retained about 3 times larger particle size of metallic nickel than the reduced NiE/MA catalyst.

Fig. 10 shows the TEM images and particle size distributions of reduced NiE/MA and Ni/MA catalysts. As shown in Fig. 10(a) and (b), the reduced NiE/MA catalyst retained small nickel particles compared to the reduced Ni/MA catalyst which retained big particles even larger than 50 nm. Furthermore, particle size distributions (Fig. 10(c)) revealed that the reduced NiE/MA catalyst exhibited narrower particle size distribution than the reduced Ni/MA catalyst, due to more uniform metal–support interaction of nickel species in the NiE/MA catalyst than in the Ni/MA catalyst. Average particle size of metallic nickel in the reduced catalysts determined by TEM analyses was similar to that calculated by the Scherrer equation (Table 2).

To compare nickel surface area and nickel dispersion of reduced NiE/MA and Ni/MA catalysts, H$_2$–TPD analyses were conducted as shown in Fig. 11. According to the previous study [50], hydrogen atoms can be located on the reduced nickel atoms as well as in the subsurface layer of nickel atoms or in the support by spillover effect. Desorption band for hydrogen atoms in the nickel subsurface layer or in the support was detected above 650 °C in the H$_2$–TPD profiles. Thus, hydrogen desorption peaks detected below 650 °C in the H$_2$–TPD profiles were only considered for the calculation of hydrogen uptake by reduced nickel atoms. For the detailed calculation, the H$_2$–TPD profiles of reduced NiE/MA and Ni/MA catalysts were deconvoluted as shown in Fig. 11. As listed in Table 3, the total amount of adsorbed hydrogen over the reduced NiE/MA catalyst was larger than that over the reduced Ni/MA catalyst. Accordingly, the reduced NiE/MA catalyst exhibited larger nickel surface area,
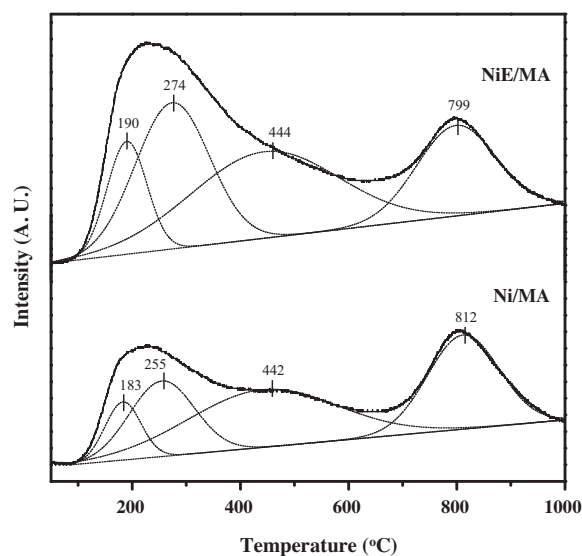

Fig. 11. H$_2$–TPD profiles of reduced NiE/MA and Ni/MA catalysts.

larger nickel dispersion, and smaller average nickel diameter than the reduced Ni/MA catalyst, in good agreement with the particle size results determined by XRD and TEM analyses. It should be noted that the reduced NiE/MA catalyst retained larger amount of strong hydrogen-binding sites than the reduced Ni/MA catalyst. It has been reported that strong hydrogen-binding sites of nickel catalyst are favorable for facilitating chemisorption of hydrogen atoms generated from dissociative adsorption of hydrogen molecules [38]. Furthermore, dissociative adsorption of methane on the reduced nickel (CH$_4$ + 2Ni → CH$_3$–Ni + H–Ni), which is known as a rate-determining step for steam reforming of methane [51], is promoted by stable adsorption of hydrogen atoms on strong hydrogen-binding sites of the reduced nickel. Thus, it is inferred that NiE/MA catalyst with many strong hydrogen-binding sites
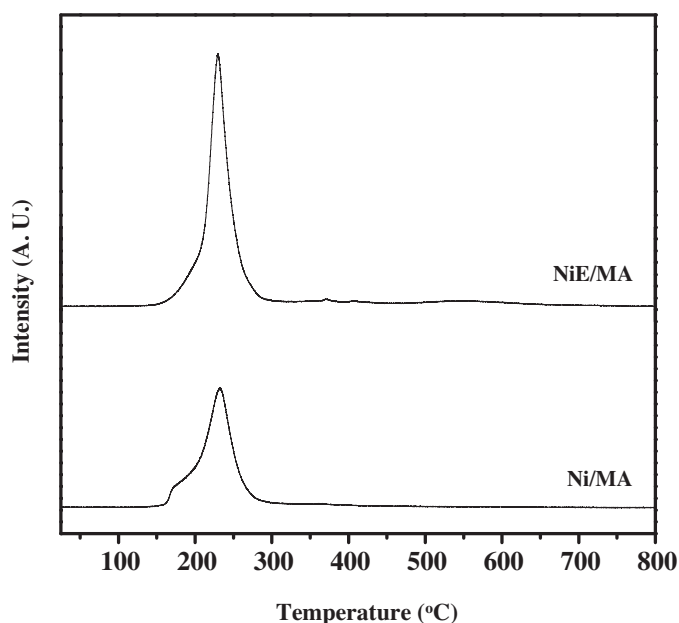
Fig. 12. CH$_4$–TPD profiles of reduced NiE/MA and Ni/MA catalysts.

Table 4
CH$_4$–TPD results of reduced NiE/MA and Ni/MA catalysts.

Catalyst	Amount of adsorbed CH$_4$ (μmol CH$_4$/g)[a]
NiE/MA	98.7
Ni/MA	50.4

[a] Calculated from peak area of CH$_4$–TPD profiles in Fig. 12.

would show larger methane adsorption capacity as well as better catalytic performance than Ni/MA catalyst.

3.5. Methane adsorption of reduced catalysts

CH$_4$–TPD analyses were conducted to measure methane adsorption capacity of reduced NiE/MA and Ni/MA catalysts as shown in Fig. 12. The amount of adsorbed CH$_4$ on the reduced catalysts was calculated from the CH$_4$–TPD profiles (Table 4). It was revealed that the reduced NiE/MA catalyst exhibited larger amount of adsorbed CH$_4$ than the reduced Ni/MA catalyst. This is because the reduced NiE/MA catalyst retained larger amount of strong hydrogen-binding sites than the reduced Ni/MA catalyst. It should be noted that the reduced NiE/MA catalyst showed 1.96 times larger methane adsorption capacity than the reduced Ni/MA catalyst, although the amount of strong hydrogen-binding sites on the reduced NiE/MA catalyst was 1.55 times larger than that on the reduced Ni/MA catalyst. This indicates that NiE/MA catalyst with efficient exposure of nickel species was favorable for methane adsorption.

3.6. Hydrogen production by steam reforming of LNG

Catalytic performance in the hydrogen production by steam reforming of LNG over NiE/MA and Ni/MA catalysts is presented in Fig. 13. LNG conversion and hydrogen yield over both NiE/MA and Ni/MA catalysts were stable during the 15 h-reaction, implying that deactivation behaviors such as nickel sintering and carbon deposition were effectively prevented over the catalysts. CHNS elemental analyses of the spent catalysts obtained after a 15 h-reaction revealed that the amount of carbon deposition was only 0.3 wt%. This means that both NiE/MA and Ni/MA catalysts were strongly resistant toward carbon deposition during the reaction due to well-

Table 5
Summarized catalytic performance data over NiE/MA and Ni/MA catalysts in the steam reforming of LNG under the same LNG conversion level (78%).

	NiE/MA	Ni/MA
LNG conversion (%)	78	78
Hydrogen yield (%)	61	58
H$_2$/CO molar ratio	17	23
CO$_2$/CO molar ratio	3.0	4.2

Table 6
Particle size of metallic nickel and degree of sintering over spent NiE/MA and Ni/MA catalysts obtained after a 24 h-reaction at 800 °C.

Catalyst	Particle size of metallic nickel (nm)[a]	Degree of sintering (%)[b]
NiE/MA	28	115
Ni/MA	86	153

[a] Average value of 100 nickel particles in TEM images of Fig. 15(a) and (b).
[b] Calculated by following equation:

Degree of sintering(%) = $\left(\frac{\text{particle size after reaction} - \text{particle size after reduction}}{\text{particle size after reduction}} \right) \times 100$ Particle sizes of metallic nickel after reduction were taken from TEM analysis results listed in Table 2.

developed mesoporosity and sufficiently exposed nickel surface, which were responsible for accelerating gasification of carbonaceous compounds.

It was observed that NiE/MA catalyst with higher nickel dispersion and larger methane adsorption was more active than Ni/MA catalyst in the steam reforming of LNG. Nickel catalyst with high nickel dispersion is known to be favorable for facilitating steam reforming of methane, because methane can be easily dissociated on many stepped nickel atoms in the catalyst [52,53]. Furthermore, the affinity of Ni/Al$_2$O$_3$ catalyst toward methane adsorption plays an important role in determining the catalytic performance, because the dissociated adsorption of methane is a rate-determining step in the steam reforming of LNG.

In order to investigate catalytic activities for steam reforming reaction (CH$_4$ + H$_2$O → CO + 3H$_2$) and water-gas shift reaction (CO + H$_2$O → CO$_2$ + H$_2$) over NiE/MA and Ni/MA catalysts, additional catalytic tests were conducted under the same LNG conversion level (78%) over NiE/MA and Ni/MA catalysts by changing contact time for both catalysts. It is interesting to note that H$_2$/CO molar ratio and CO$_2$/CO molar ratio over NiE/MA catalyst were smaller than those over Ni/MA catalyst (Table 5) under the same LNG conversion level. Considering high hydrogen yield of NiE/MA catalyst compared to Ni/MA catalyst, it can be inferred NiE/MA catalyst was relatively effective for facilitating steam reforming reaction rather than water–gas shift reaction.

Fig. 14 shows the catalytic performance of NiE/MA and Ni/MA catalysts under severe reaction condition (800 °C). Both NiE/MA and Ni/MA catalysts showed the enhanced LNG conversion and hydrogen yield at 800 °C compared to those at 550 °C. It should be noted that no significant catalyst deactivation was observed over the catalysts during the 24 h-reaction, even though high reaction temperature was employed. Particle sizes of metallic nickel over the spent catalysts obtained after a 24 h-reaction were determined by TEM images (Fig. 15), as listed in Table 6. It was found that particle size of metallic nickel over both NiE/MA and Ni/MA catalysts considerably increased after the reaction due to high reaction temperature, which accelerated nickel sintering. However, NiE/MA catalyst (Fig. 15(a)) still retained smaller nickel particle size than Ni/MA catalyst (Fig. 15(b)) after the steam reforming reaction. Degree of sintering over NiE/MA catalyst was also smaller than that over Ni/MA catalyst (Table 6), representing that NiE/MA catalyst retained stronger resistance toward nickel sintering than Ni/MA catalyst even under high reaction temperature condition. In conclu-
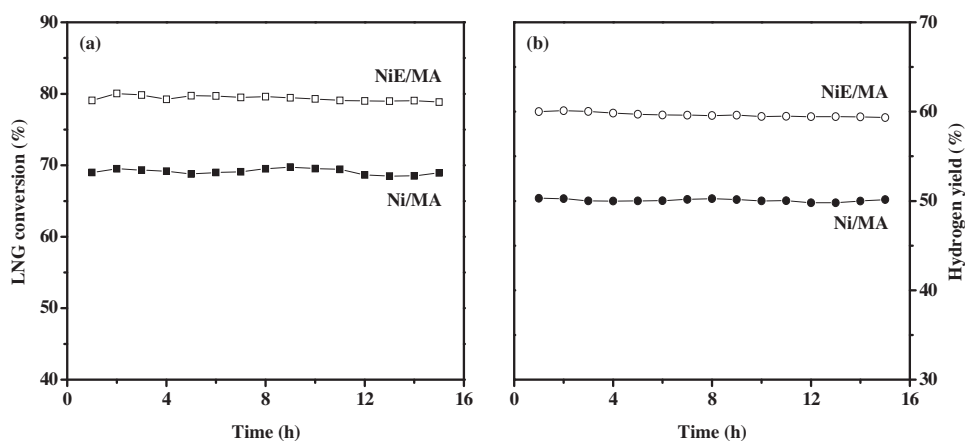
Fig. 13. (a) LNG conversion and (b) hydrogen yield with time on stream in the steam reforming of LNG over NiE/MA and Ni/MA catalysts at 550 °C.
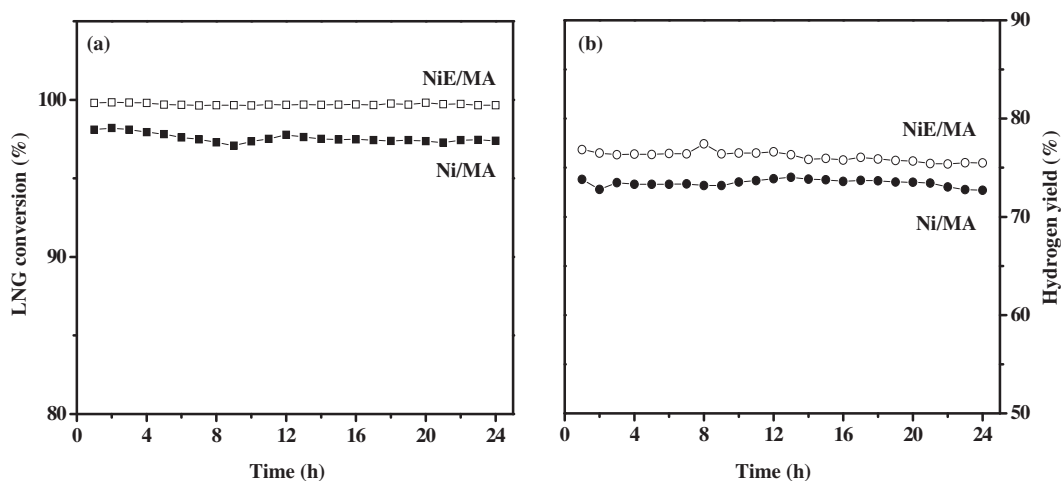

Fig. 14. (a) LNG conversion and (b) hydrogen yield with time on stream in the steam reforming of LNG over NiE/MA and Ni/MA catalysts at 800 °C.
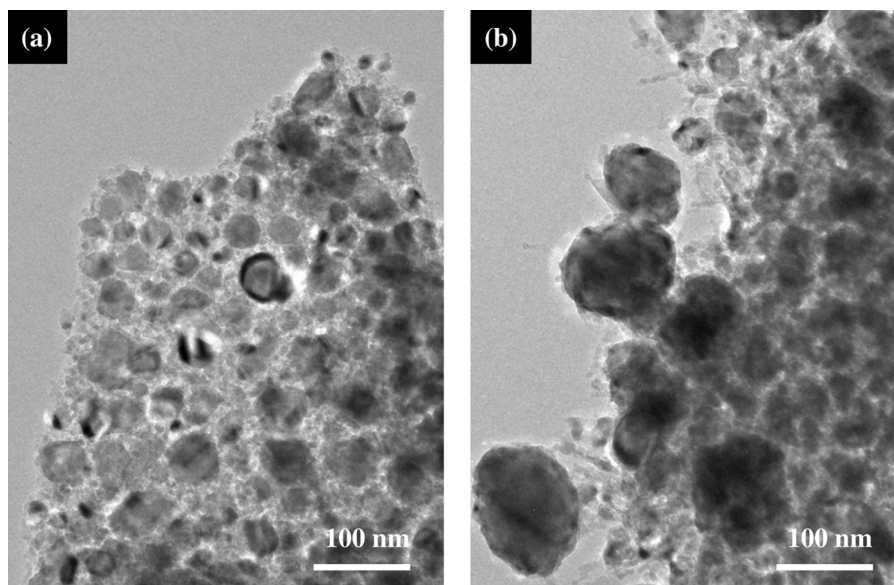

Fig. 15. TEM images of spent (a) NiE/MA catalyst and (b) Ni/MA catalyst obtained after a 24 h-reaction at 800 °C.

sion, NiE/MA catalyst served as an efficient catalyst in the hydrogen production by steam reforming of LNG.

4. Conclusions

A mesoporous Ni/Al_2O_3 catalyst was prepared by an EDTA-assisted impregnation method (NiE/MA), and it was applied to the hydrogen production by steam reforming of LNG. A mesoporous Ni/Al_2O_3 catalyst was also prepared by a conventional impregnation method (Ni/MA) for comparison purpose. EDTA-assisted impregnation applied for the preparation of NiE/MA catalyst was achieved via the Coulombic interaction between positively-charged hydroxyl groups ($-OH^{2+}$) on MA support and $Ni(EDTA)^{2-}$ complex anions. As a result, textural properties and metal–support interaction of NiE/MA catalyst were enhanced compared to those of Ni/MA catalyst. The reduced NiE/MA catalyst retained smaller nickel particles and showed higher nickel dispersion than the reduced Ni/MA catalyst. Furthermore, the amount of adsorbed CH_4 over the reduced NiE/MA catalyst was larger than that over the reduced Ni/MA catalyst. In the steam reforming of LNG, consequently, NiE/MA catalyst with larger methane adsorption capacity exhibited better catalytic performance than Ni/MA catalyst. It was found that NiE/MA catalyst was relatively more active for steam reforming reaction rather than water–gas shift reaction compared to Ni/MA catalyst under the same LNG conversion level. NiE/MA catalyst also exhibited stronger resistance toward nickel sintering during the high-temperature (800 °C) steam reforming of LNG than Ni/MA catalyst.

Acknowledgement

References

[1] M. Poliakoff, P. Licence, Nature 450 (2007) 810–812.
[2] J. Goldemberg, Science 315 (2007) 808–810.
[3] I. Dincer, Int. J. Hydrog. Energy 37 (2012) 1954–1971.
[4] V. Palma, F. Castaldo, P. Ciambelli, G. Iaquaniello, Appl. Catal. B: Environ. 145 (2014) 73–84.
[5] M. Balat, Int. J. Hydrog. Energy 33 (2008) 4013–4029.
[6] K. Mazloomi, C. Gomes, Renew. Sustain. Energy Rev. 16 (2012) 3024–3033.
[7] C.-J. Winter, Int. J. Hydrog. Energy 34 (2009) S1–S52.
[8] K. Geissler, E. Newson, F. Vogel, T.-B. Truong, P. Hottinger, A. Wokaun, Phys. Chem. Chem. Phys. 3 (2001) 289–293.
[9] B.T. Schädel, M. Duisberg, O. Deutschmann, Catal. Today 142 (2009) 42–51.
[10] K.M.K. Yu, W. Tong, A. West, K. Cheung, T. Li, G. Smith, Y. Guo, S.C.E. Tsang, Nat. Commun. 3 (2012) 1–7.
[11] C. Wu, P.T. Williams, Environ. Sci. Technol. 44 (2010) 5993–5998.
[12] A.C. Basagiannis, X.E. Verykios, Int. J. Hydrog. Energy 32 (2007) 3343–3355.
[13] A. Iriondo, V.L. Barrio, J.F. Cambra, P.L. Arias, M.B. Guemez, M.C. Sanchez-Sanchez, R.M. Navarro, J.L.G. Fierro, Int. J. Hydrog. Energy 35 (2010) 11622–11633.
[14] M.H. Halabi, M.H.J.M. Croon, J. Schaaf, P.D. Cobden, J.C. Schouten, Appl. Catal. A: Gen. 389 (2010) 68–79.
[15] D.A.J.M. Ligthart, R.A. Santen, E.J.M. Hensen, J. Catal. 280 (2011) 206–220.
[16] D. Homsi, S. Aouad, C. Gennequin, A. Aboukaïs, E. Abi-Aad, Int. J. Hydrog. Energy 39 (2014) 10101–10107.
[17] A. Gallo, C. Pirovano, P. Ferrini, M. Marelli, R. Psaro, S. Santangelo, G. Faggio, V.D. Santo, Appl. Catal. B: Environ. 121–122 (2012) 40–49.
[18] L.S.F. Feio, C.E. Hori, S. Damyanova, F.B. Noronha, W.H. Cassinelli, C.M.P. Marques, J.M.C. Bueno, Appl. Catal. A: Gen. 316 (2007) 107–116.
[19] C. Shi, P. Zhang, Appl. Catal. B: Environ. 115–116 (2012) 190–200.
[20] V.B. Mortola, S. Damyanova, D. Zanchet, J.M.C. Bueno, Appl. Catal. B: Environ. 107 (2011) 221–236.
[21] M. Kusche, F. Agel, N.N. Bhriain, A. Kaftan, M. Laurin, J. Libuda, P. Wasserscheid, ChemSusChem 7 (2014) 2516–2526.
[22] A.L.M. Silva, J.P. Breejen, L.V. Mattos, J.H. Bitter, K.P. Jong, F.B. Noronha, J. Catal. 318 (2014) 67–74.
[23] G. Garbarino, P. Riani, M.A. Lucchini, F. Canepa, S. Kawale, G. Busca, Int. J. Hydrog. Energy 38 (2013) 82–91.
[24] I.H. Son, S.J. Lee, A. Soon, H.-Y. Roh, H. Lee, Appl. Catal. B: Environ. 134–135 (2013) 103–109.
[25] S.Y. Lee, H. Lim, H.C. Woo, Int. J. Hydrog. Energy 39 (2014) 17645–17655.
[26] J. Sehested, N.W. Larsen, H. Falsig, B. Hinnemann, Catal. Today 228 (2014) 22–31.
[27] P.K. Sharma, N. Saxena, A. Bhatt, C. Rajagopal, P.K. Roy, Catal. Sci. Technol. 3 (2013) 1017–1026.
[28] C. Melchor-Hernández, A. Gómez-Cortés, G. Díaz, Fuel 107 (2013) 828–835.
[29] Y. Bang, J.G. Seo, M.H. Youn, I.K. Song, Int. J. Hydrog. Energy 37 (2012) 1436–1443.
[30] Z. Wang, X. Shao, X. Hu, G. Parkinson, K. Xie, D. Dong, C.-Z. Li, Catal. Today 228 (2014) 199–205.
[31] Y. Bang, S.J. Han, J.G. Seo, M.H. Youn, J.H. Song, I.K. Song, Int. J. Hydrog. Energy 37 (2012) 17967–17977.
[32] J. Remón, J.A. Medrano, F. Bimbela, L. García, J. Arauzo, Appl. Catal. B: Environ. 132–133 (2013) 433–444.
[33] J.A. Calles, A. Carrero, A.J. Vizcaíno, L. García-Moreno, Catal. Today 227 (2014) 198–206.
[34] R.-X. Yang, K.-H. Chuang, M.-Y. Wey, Int. J. Hydrog. Energy 39 (2014) 19494–19501.
[35] K. Al-Dalama, B. Aravind, A. Stanislaus, Appl. Catal. A: Gen. 296 (2005) 49–53.
[36] J. Ryczkowski, Vib. Spectrosc. 43 (2007) 203–209.
[37] A.I. Tsyganok, K. Suzuki, S. Hamakawa, K. Takehira, T. Hayakawa, Catal. Lett. 77 (2001) 75–86.
[38] Y. Bang, S.J. Han, J. Yoo, J.H. Choi, J.K. Lee, J.H. Song, J. Lee, I.K. Song, Appl. Catal. B: Environ. 148–149 (2014) 269–280.
[39] T.-Y. Wei, C.-H. Chen, H.-C. Chien, S.-Y. Lu, C.-C. Hu, Adv. Mater. 22 (2010) 347–351.
[40] A.E. Gash, T.M. Tillotson, J.H. Satcher Jr., J.F. Poco, L.W. Hrubesh, R.L. Simpson, Chem. Mater. 13 (2001) 999–1007.
[41] R.A. Shawabkeh, M. Al-Harthi, S.M. Al-Ghamdi, Energy Sources Part A 36 (2014) 93–103.
[42] M.A. Zaitoun, C.T. Lin, J. Phys. Chem. B 101 (1997) 1857–1860.
[43] K.S.W. Sing, D.H. Everett, R.A.W. Haul, L. Moscou, R.A. Pierotti, J. Rouquerol, T. Siemieniewska, Pure Appl. Chem. 57 (1985) 603–619.
[44] J.G. Seo, M.H. Youn, K.M. Cho, S. Park, I.K. Song, J. Power Sources 173 (2007) 943–949.
[45] P. Kim, Y. Kim, H. Kim, I.K. Song, J. Yi, J. Mol. Catal. A: Chem. 231 (2005) 247–254.
[46] J.M. Rynkowski, T. Paryczak, M. Lenik, Appl. Catal. A: Gen. 106 (1992) 73–82.
[47] G. Li, L. Hu, J.M. Hill, Appl. Catal. A: Gen. 10 (2006) 16–24.
[48] J.G. Seo, M.H. Youn, I.K. Song, Int. J. Hydrog. Energy 34 (2009) 1809–1817.
[49] S. Natesakhawat, R.B. Watson, X. Wang, U.S. Ozkan, J. Catal. 234 (2005) 496–508.
[50] S. Velu, S.K. Gangwal, Solid State Ion. 177 (2006) 803–811.
[51] D.L. Trimm, Stud. Surf. Sci. Catal. 36 (1987) 39–50.
[52] J.R. Rostrup-Nielsen, J.K. Nørskov, Top. Catal. 40 (2006) 1–4.
[53] Y. Bang, J. Lee, S.J. Han, J.G. Seo, M.H. Youn, J.H. Song, I.K. Song, Int. J. Hydrog. Energy 37 (2012) 11208–11217.